Efficient Modulation of Magnon Conductivity in Y3Fe5 O12 Using Anomalous Spin Hall Effect of a Permalloy Gate Electrode

Santos, O. Alves; Feringa, F.; Das, K. S.; Youssef, J. Ben; Van Wees, B. J.

Published in:
Physical Review Applied

DOI:
10.1103/PhysRevApplied.15.014038

Publication date:
2021

Efficient Modulation of Magnon Conductivity in $Y_3Fe_5O_{12}$ Using Anomalous Spin Hall Effect of a Permalloy Gate Electrode

O. Alves Santos,[1,*] F. Feringa,[1] K.S. Das,[1] J. Ben Youssef,[2] and B.J. van Wees[1]

[1] *Physics of Nanodevices, Zernike Institute for Advanced Materials, University of Groningen, Nijenborgh 4, Groningen, AG 9747, Netherlands*

[2] *Université de Bretagne Occidentale, LabSTICC/CNRS-UMR 6285, 6 Avenue Le Gorgeu, Brest Cedex 29238, France*

(Received 8 June 2020; revised 2 October 2020; accepted 23 December 2020; published 21 January 2021)

We report the control of the modulation efficiency of the magnon conductivity in yttrium iron garnet (YIG) using magnon spin injection from a ferromagnetic metal permalloy (Py) used as a modulator in a three-terminal magnon transistor geometry. The modulation efficiency is estimated by means of nonlocal spin-transport measurements between platinum injector and detector strips. A charge current is sent through the Py modulator to create a spin accumulation at the YIG-Py interface via the spin Hall effect and the anomalous spin Hall effect (ASHE). We observe an enhancement of the modulation efficiency for the electrically generated magnons from 2.5%/mA at 10 mT to 4.7%/mA for magnetic fields higher than 50 mT. That enhancement is attributed to the ASHE, which is maximized when the Py magnetization is perpendicular to the charge current. However, the modulation efficiency of the thermally generated magnons exhibits an opposite behavior, 12.0%/mA at 10 mT to 6.6%/mA at 50 mT, which disagrees with what we expect from the ASHE contribution to the modulation.

DOI: 10.1103/PhysRevApplied.15.014038

I. INTRODUCTION

One of the major goals of spintronics is the efficient generation and manipulation of the spin degree of freedom, e.g., by using spin currents [1–3]. In the ferrimagnetic insulator yttrium iron garnet (YIG), the spin current, i.e., the flow of spin angular momentum does not occur via the transport of conduction electrons, but via spin waves or magnons, i.e., the quanta of spin waves in a magnetic material [4–8]. The excited magnons in YIG can transmit electrical signals over distances as large as 40 μm [9–14]. The magnon conductivity (σ_m) in YIG can be modulated in two ways. First, by increasing or decreasing the magnon chemical potential via spin injection produced by the spin Hall effect (SHE) [15,16], when a charge current (I_{dc}) is applied in the middle-modulator terminal in the three-terminal magnon transistor, developed by Cornelissen *et al.* [17]. Second, via the magnetic gating effect (MGE) [18], where the magnon relaxation in the YIG channel is tuned by the relative angle between the magnetization of YIG and the magnetic modulator (gate). It was found that when the magnetizations are parallel to each other more magnons are absorbed by the gate, decreasing the transmission of magnons between the platinum (Pt) injector and detector strips [18].

Besides the spin injection due to the longitudinal spin-charge coupling [19–21], permalloy (Py) is a ferromagnetic metal, which can convert a charge current into a transverse spin current by the Py magnetization (M_{Py}) independent SHE, and the magnetization-dependent anomalous spin Hall effect (ASHE), which is maximized when M_{Py} is perpendicular to the charge-current direction [22–24]. Thereby, Py can be used as a transverse spin current injector and detector via SHE and ASHE [25–27]. Moreover, hybrid magnetic structures, such as YIG-Py, have proven to be the subject of great interest in the study of spin-wave coupling, spin-wave propagation, and their promising capacity to integrate magnonic devices with the mainstream microwave electronics, quantum information, and photonics [28–38].

In this paper, we demonstrate the control of the magnon conductivity in YIG, driven by the combined SHE and ASHE spin injection using Py as a modulator in a three-terminal magnon transistor. In the absence of a charge current in the Py gate we observe a MGE with modulation at least 4 times larger than previously reported [18]. Applying a charge current through the Py strip, we obtain an enhancement of the spin-current-controlled modulation from 2.5%/mA at 10 mT to 4.7%/mA at fields higher than 50 mT on the electrically generated magnons. That enhancement is attributed to the spin accumulation in the modulator due to the ASHE

*o.alves.santos@rug.nl

contribution. However, we observe the opposite behavior for thermally generated magnons, the maximum modulation efficiency of 12.0%/mA is observed at 10 mT, while at fields higher than 50 mT we obtain 6.6%/mA. The last observation is not in agreement with what we expect from the ASHE contribution on the thermally generated magnon modulation.

II. EXPERIMENTAL SETUP

The devices consist of a pair of Pt injector and detector strips with dimensions of (18×0.3) μm separated by a distance of 2 μm (center to center) and a Py middle modulator strip, with a length of 22 μm and varying width from 300 to 700 nm, deposited on top of a 26-nm-thick LPE-YIG film grown onto GGG substrate. All Pt and Py strips have thicknesses of 7 and 12 nm, respectively. See Sec. I within the Supplemental Material for fabrication details [39]. Figure 1(a) shows the schematic illustration of the experimental geometry.

A charge current (I_{ac}) is applied to the injector with an amplitude of 500 μA at a frequency of 17.777 Hz. The current in the injector creates a spin accumulation (μ_s) at the interface of YIG-Pt via the SHE, with polarization along $\hat{y}$ direction. Only the component of μ_s parallel to the net YIG magnetization (M_{YIG}) produces nonequilibrium magnons in the YIG, which diffuse through the YIG film, therefore, the injected magnons follow a $\cos\alpha$ dependence. At the detector, the magnons produce a spin accumulation parallel to M_{YIG}. Once again, only the spin accumulation parallel to $\hat{y}$ direction produces a charge current in the Pt electrode via the reciprocal effect, the inverse spin Hall effect (ISHE) [40,41], i.e., $\cos\alpha$ dependence of the detected magnons. This mechanism corresponds to the electrical injection and detection of magnons, illustrated in Fig. 1(a). The detected voltage is a product of both effects, resulting in $V^{1\omega} \propto \cos^2\alpha$, which is measured in the first-harmonic ($1f$) response [9,10]. In addition to that, a second-harmonic response ($2f$) is measured, corresponding to the thermally generated magnons. In this case, the thermally generated magnons do not depend on the spin accumulation in the injector, since they are produced by the spin Seebeck effect driven by the thermal gradient created by the Joule heating in the injector [42–44]. However, the mechanism of detection is still the same, therefore the voltage measured at the $2f$ response corresponds to $V^{2\omega} \propto \cos\alpha$ [9,10].

Figure 1(b) shows the $1f$ response as a function of the angle for a device without a modulator for an external magnetic field (B) of 60 mT, the inset shows the electrical connections. The magnetic field is swept for fixed $\alpha = 0^\circ$ and $\alpha = 90^\circ$, and the $1f$ response is measured, as shown in Fig. 1(c). For $\alpha = 0^\circ$ the voltage remains constant except below (approximately equal to 6 mT), where M_{YIG} do not follow the external magnetic field, and the voltage goes to a minimum value. The magnetic-field-dependent measurements of the $2f$ response are shown in Fig. 1(c), following the $\cos\alpha$ dependence. The measured step in Fig. 1(e), corresponds to the change of the M_{YIG} direction. The $1f$ and $2f$ voltages decrease by increasing the magnetic field, this is expected due to the magnetic field dependence of the spin-diffusion length of YIG [45].

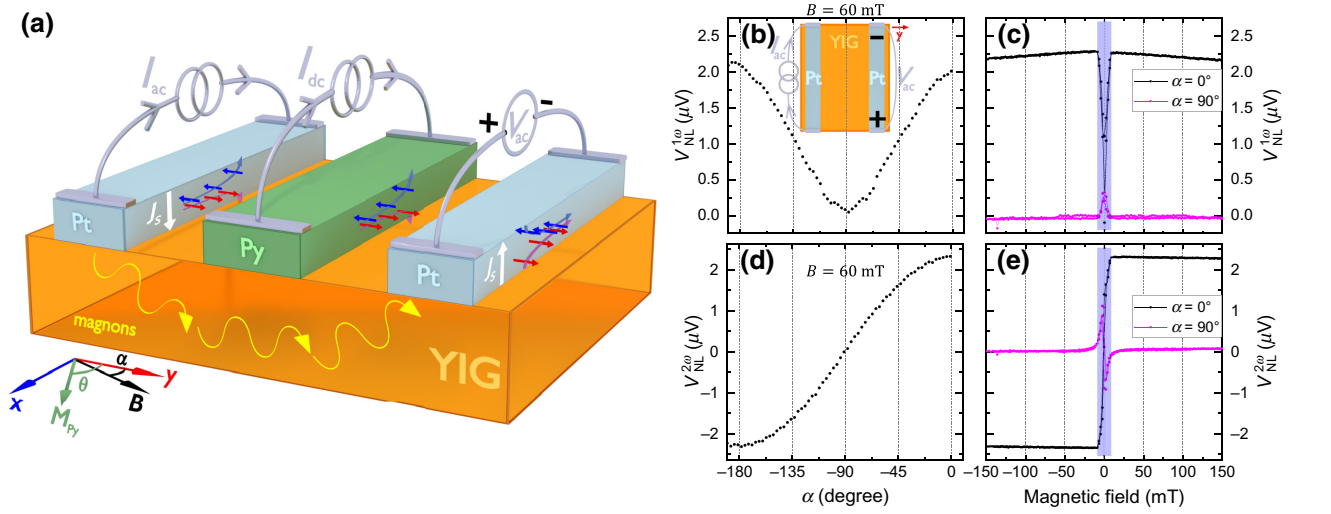

FIG. 1. (a) Schematic illustration showing the electrical connections of the transistor device and the phenomena involved. The injection of magnons via SHE produced by a charge current (I_{ac}) in the injector, transmission of magnons in YIG, the conversion of spin current into a charge current by ISHE in the detector and the applied charge current (I_{dc}) in the modulator. (b),(c) First-harmonic-dependent voltage as a function of the relative angle α between $\vec{B}$ and $\hat{y}$, and magnetic field strength, respectively, for the reference sample without the modulator. The inset in (b) shows the electrical configuration of the measurements. (d),(e) Second-harmonic-dependent measurements.

Following the analysis from Cornelissen *et al.* [9], the voltages measured on the detector can be written as nonlocal resistances $R_{\rm NL}$, expressed in terms of the angle (α) between $\hat{y}$ axis and the external magnetic field $\vec{B}$ for the $1f$ and $2f$ harmonic as,

$$R_{\rm NL}^{1\omega} = \frac{V^{1\omega}(\alpha)}{I_{\rm ac}} = C_1\sigma_m \cos^2\alpha = A^{1\omega}\cos^2\alpha, \quad (1)$$

$$R_{\rm NL}^{2\omega} = \frac{V^{2\omega}(\alpha)}{I_{\rm ac}^2} = C_2\sigma_m \cos\alpha = A^{2\omega}\cos\alpha, \quad (2)$$

where σ_m is the magnon conductivity, C_1 and C_2 are the charge-to-magnon conversion parameters and $A^{1\omega}$ and $A^{2\omega}$ represent the maximum amplitude of the nonlocal resistances for electrical and thermal injection of magnons, respectively [9]. Due to the strong spin-orbit interaction in the Pt strip, the large spin-mixing conductance at the YIG-Pt interface and the injected magnon density, which is proportional to the charge current. The injector acts like a low-impedance magnon source, while the detector as a low-impedance magnon drain. Therefore, we can express the magnon conductivity σ_m in this simple form.

III. ($I_{\rm dc} = 0$)—MAGNETIC GATING EFFECT

The Py strip placed between the injector and detector absorbs part of the magnons created by the injector at the YIG-Py interface, even in the absence of an applied charge current. Due to the shape anisotropy, the magnetization of Py has an easy axis along $\hat{x}$ ($\theta = -90°, 90°$), where θ is the angle between the $\hat{y}$ axis and the $\vec{M}_{\rm Py}$. In agreement with previous experiments, the $M_{\rm Py}$ rotates freely with respect to the $M_{\rm YIG}$ in the YIG film, demonstrated via anomalous magnetoresistance measurements on the Py strip, which indicates a weak coupling interaction between Py and YIG [22,23]. An external magnetic field of $B \approx 50$ mT is required to fully align $M_{\rm Py}$ along the hard axis, for a 700-nm-wide Py strip. The amount of magnons absorbed depends on the relative orientation between $M_{\rm YIG}$ and $M_{\rm Py}$, which is illustrated in Figs. 2(a) and 2(b) as a higher or lower regime of the transport of magnons for an external magnetic field along the $\hat{y}$ direction. The control of magnon transport by a magnetic modulator is called magnetic gating effect [18]. Therefore, varying the magnetic field strength along the hard axis the MGE will produce an enhancement of the magnon transport between Pt injector and detector strips for $B < 50$ mT [18]. Figures 2(c) and 2(d), show a magnified region of the field scan measurement of $R_{\rm NL}^{1\omega}$ and $R_{\rm NL}^{2\omega}$ for different Py widths (w). In order to quantify the magnetic gating effect, we parametrize the modulation by MGE as $\delta_{\rm MGE}^{1\omega(2\omega)}$, by

$$\delta_{\rm MGE}^{1\omega(2\omega)} = \frac{\Delta R_{\rm tot}^{1\omega(2\omega)}}{R_{\rm sat}^{1\omega(2\omega)}}, \quad (3)$$

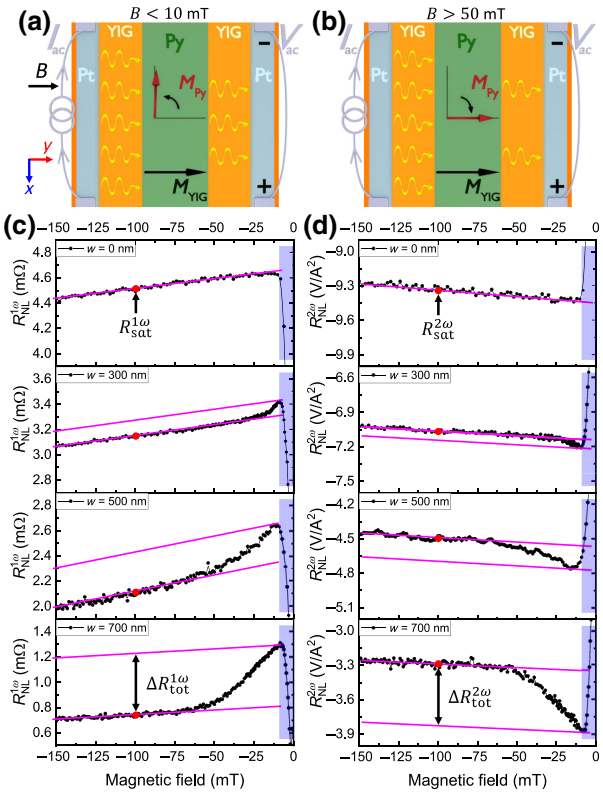

FIG. 2. Presence of the Py modulator produces the MGE, where the absorption of magnons is lower (a), or higher (b), due to the relative orientation between the magnetizations of the Py strip and the YIG layer. (c),(d) Enlargement of the nonlocal resistances for different modulator widths (w) for $1f$ and $2f$, respectively.

where $R_{\rm sat}^{1\omega(2\omega)}$ is the value of $R_{\rm NL}^{1\omega(2\omega)}$ at 100 mT, and $\Delta R_{\rm tot}^{1\omega(2\omega)}$ is the difference in m$\Omega(V/A^2)$ of the nonlocal resistance between higher and lower regimes of magnon transport for 1ω (2ω). The MGE parameters are summarized in Table I. An enhancement of 65% for the $1f$ signal and 16% for the $2f$ signal are obtained for a modulator width of 700 nm. The observed values of the MGE are at least 4 times larger than those obtained in the 210-nm-thick YIG by Das *et al.* [18]. It is expected for the thinner YIG used in this paper, where the interface interaction becomes more relevant to the magnon conductivity. The width dependence of $R_{\rm sat}^{1\omega(2\omega)}$, $\Delta R_{\rm tot}^{1\omega,(2\omega)}$, and $\delta_{\rm MGE}^{1\omega(2\omega)}$ are shown in Sec. II of the Supplemental Material [39].

The magnetic gating effect modulates the total number of magnons that reach the detector without the need of any applied charge current in the modulator. Meaning that the magnons in YIG are in (almost) equilibrium with the Py layer, and no spin accumulation is produced at the YIG-Py interface. Therefore, the MGE is a different mechanism of magnon transport modulation than the spin-current-controlled modulation reported by Ref. [17].

TABLE I. Values of nonlocal resistances R_{sat} and $\delta_{MGE}^{1\omega(2\omega)}$ defined in Eq. (3), for the first and second harmonic, respectively, as a function of the Py width.

Width (nm)	$R_{sat}^{1\omega}$ (mΩ)	$\delta_{MGE}^{1\omega}$ (%)	$R_{sat}^{2\omega}$ (V/A^2)	$\delta_{MGE}^{2\omega}$ (%)
0	4.51 ± 0.01	0	9.32 ± 0.02	0
300	3.15 ± 0.01	3.9	7.06 ± 0.01	1.2
500	2.10 ± 0.03	15.4	4.59 ± 0.03	4.4
700	0.74 ± 0.01	65.4	3.29 ± 0.02	16.2

By applying a charge current in the modulator, a superposition of the quasiequilibrium modulation due to the MGE and the nonequilibrium spin-current modulation produced by SHE and ASHE is expected.

IV. ($I_{dc} \neq 0$)—ASHE CONTRIBUTION TO THE MAGNON CONDUTIVITY MODULATION

Cornelissen *et al.* [17] demonstrated that the magnon spin conductivity in YIG can be controlled by a charge current sent through the modulator, increasing or decreasing the number of magnons in the YIG channel proportional to the spin accumulation produced at the YIG-modulator interface. In addition to a sizable and magnetization-independent SHE, Py possesses the ASHE, which corresponds to a magnetization-dependent term in the spin accumulation (μ_s^{Py}) produced in the Py strip [19–23]. Taking into account both the contributions for μ_s^{Py}, one can write the magnon conductivity in the YIG channel due to the Py modulator as,

$$\sigma_m(\alpha) = \sigma_m^0 \Delta\sigma_J I_{dc}^2 + \Delta\sigma_{SHE} I_{dc} \cos\alpha + \Delta\sigma_{ASHE} I_{dc} \cos\theta \cos(\alpha - \theta), \quad (4)$$

where σ_m^0 is the magnon conductivity without a charge current, $\Delta\sigma_J$ and $\Delta\sigma_{SHE}$ parametrize the efficiency of modulation by Joule heating and SHE injection of magnons, respectively. The last term in Eq. (4) represents the ASHE contribution, where $\Delta\sigma_{ASHE}$ is the efficiency of modulation. The angular dependency of the ASHE term arises from the magnitude of μ_s^{ASHE}, orthogonal between both M_{Py} and I_{dc} directions, i.e., $\cos\theta$, and the projection of the spin accumulation on the magnetization of YIG, $\cos(\alpha - \theta)$. Plugging Eq. (4) into Eqs. (1) and (2), we obtain the nonlocal resistance, which takes into account the SHE and ASHE modulation. In addition to that, we can write the angular dependence of MGE, which modulates the $A^{1\omega}$ and $A^{2\omega}$ proportional to the relative angle between M_{Py} and M_{YIG}. Therefore one can write the nonlocal resistances as,

$$R_{NL}^{1\omega}(\text{m}\Omega) = A^{1\omega}\left[1 - \delta_{MGE}^{1\omega}\cos(\theta - \alpha)\right]\cos^2\alpha + B_{SHE}^{1\omega}\cos^3\alpha + B_{ASHE}^{1\omega}\cos^2\alpha\cos\theta\cos(\theta - \alpha), \quad (5)$$

$$R_{NL}^{2\omega}(V/A^2) = A^{2\omega}\left[1 - \delta_{MGE}^{2\omega}\cos(\theta - \alpha)\right]\cos\alpha + B_{SHE}^{2\omega}\cos^2\alpha + B_{ASHE}^{2\omega}\cos\alpha\cos\theta\cos(\theta - \alpha), \quad (6)$$

where $\delta_{MGE}^{1\omega(2\omega)}$ parametrize the modulation of magnon transport due to the MGE, defined in Eq. 3. The amplitudes $A^{1\omega}$ and $A^{2\omega}$ are proportional to I_{dc}^2 as a consequence of the modulator heating effects on the measured nonlocal resistances [46], while $B_{SHE}^{1\omega(2\omega)} \propto I_{dc}$ is the modulation amplitude due to the $\Delta\sigma_{SHE}$. The last term of Eqs. (5) and (6) stems from the modulation of the magnon conductivity driven by the ASHE, where $B_{ASHE}^{1\omega(2\omega)} \propto I_{dc}$, is the modulation amplitude due to $\Delta\sigma_{ASHE}$.

Here we can analyze the angular dependency for two distinct regimes: (i) for $|B| < 10$ mT, the magnetization of Py is close to $\pm 90°$, hence, minimum absorption of MGE and minimum contribution of ASHE on the spin accumulation. Therefore, Eq. (5) is reduced to $R_{NL}^{1\omega} = A^{1\omega}\cos^2\alpha + B_{SHE}^{1\omega}\cos^3\alpha$; (ii) for fields higher than 50 mT, both magnetizations follow the external field, i.e., $\theta \approx \alpha$. As a consequence, Eq. (5) becomes $R_{NL}^{1\omega} = A^{1\omega}\left(1 - \delta_{MGE}^{1\omega}\right)\cos^2\alpha + \left(B_{SHE}^{1\omega} + B_{ASHE}^{1\omega}\right)\cos^3\alpha$. The same analysis is applicable to Eq. (6). Consequently, the ASHE contribution, will enhance the modulation efficiency for fields higher than 50 mT, i.e., increase $B^{1\omega}\cos^3\alpha$ and $B^{2\omega}\cos^2\alpha$, for the $1f$ and $2f$ response. Moreover, the shape anisotropy present in the Py strip, enables us to tune the magnon transport modulation efficiency by turning the ASHE component on and off as a function of the magnetic field strength.

Qualitatively, one can quantify the contribution of the ASHE on the total spin accumulation by measuring the $1f$ response of the nonlocal resistance at the Pt detector using the Py strip as the injector. This measurement is presented in the appendix. The ratio between $1f$ nonlocal resistances at 60 and 10 mT correspond qualitatively to the spin accumulation at the YIG-Py interface caused by ASHE+SHE and SHE, respectively [23]. The obtained value is $R_{NL}^{1\omega}(60\ mT)/R_{NL}^{1\omega}(10\ \text{mT}) \approx 1.7$, for the 700-nm-wide Py, Figs. 6(a) and 6(b). Therefore, we expect an enhancement of the magnon transport modulation efficiency close to that value for first- and second-harmonic measurements.

A. Modulation efficiency of electrically and thermally generated magnons

The angular-dependent measurements of the first- and second-harmonic nonlocal resistances at 10 mT [60 mT]

for different applied charge currents are shown in Figs. 3(a) and 3(b) [(e) and (f)], for a 700-nm-wide Py modulator. The solid lines represent the best fit obtained using Eqs. (5) and (6), assuming $\theta \approx \pm 90^\circ$ [$\theta \approx \alpha$]. Figures 3(c) and 3(g) show the parameters $A^{1\omega}$ and $A^{2\omega}$ as a function of the charge current in the modulator, extracted from the fitted curves at 10 and 60 mT. In both measurements, the quadratic dependence with respect to the charge current of parameters $A^{1\omega}$ and $A^{2\omega}$ can be seen, as a result of the thermal effects. The quadratic dependence of $A^{2\omega}$ remains the same for 10 and 60 mT, $A^{2\omega} \approx -0.76\ (V/A^2)/\text{mA}^2$. However, we obtain an enhancement for $A^{1\omega}$ from 69 $\mu\Omega/\text{mA}^2$ at 10 mT to 192 $\mu\Omega/\text{mA}^2$ at 60 mT. The opposite sign of the quadratic dependency occurs mainly due to the opposite temperature dependence of electrically and thermally generated magnon signals, more details can be found in Ref. [17,47]. The Joule heating in the magnetic modulator can also affect the MGE efficiency. The observed enhancement of $A^{1\omega}$ can be a result of the lower magnon absorption by MGE caused by the higher temperature at the YIG-Py interface. The complete analysis of the temperature dependence of MGE needs further investigation in future experiments.

Figures 3(d) and 3(h) show the charge-current dependence of $B^{1\omega}$ and $B^{2\omega}$ extracted from the best fit of Eqs. (5) and (6). Parameter $B^{1\omega}$ shows an offset in Figs. 3(d) and 3(h). This offset corresponds to an asymmetry observed between positive and negative field even in the absence of a charge current. A similar asymmetry was also reported by Wimmer *et al.* [48], the responsible mechanism is still not clear. The SHE and ASHE modulation contribution show a linear behavior with respect to the I_{dc}. The slope dB/dI_{dc} describes the magnitude of the spin-current modulation. The magnitude of the electrically generated magnon modulation for 10 and 60 mT is obtained as $dB^{1\omega}_{10\text{ mT}}/dI_{\text{dc}} = -29 \pm 3\ \mu\Omega/\text{mA}$ and $dB^{1\omega}_{60\text{ mT}}/dI_{\text{dc}} = -37 \pm 3\ \mu\Omega/\text{mA}$, respectively. Here we introduce the modulation efficiency as $\eta = dB/dI_{\text{dc}}/A_0$, where A_0 is the nonlocal resistance at $I_{\text{dc}} = 0$. We obtain, $\eta^{1\omega}_{10\text{ mT}} = 2.5 \pm 0.2\%/\text{mA}$ and $\eta^{1\omega}_{60\text{ mT}} = 4.7 \pm 0.2\%/\text{mA}$.

The enhancement is attributed to the ASHE contribution of the total spin accumulation at the YIG-Py interface for $|B| > 50$ mT, which confirms that the sign of the spin accumulation due to the ASHE is the same as of the SHE [22]. The ratio obtained between the modulation efficiency at 60 and 10 mT is $\eta^{1\omega}_{60\text{ mT}}/\eta^{1\omega}_{10\text{ mT}} \approx 1.9$, which corroborates with the ratio of the ASHE contribution obtained in Figs. 6(a) and 6(b) of $R^{1\omega}_{60\text{ mT}}/R^{1\omega}_{10\text{ mT}} \approx 1.7$. In contrast, the slope of $B^{2\omega}$ decreases from $dB^{2\omega}_{10\text{ mT}}/dI_{\text{dc}} = 0.48 \pm 0.03\ \text{V}/A^2/\text{mA}$ at 10 mT to $dB^{2\omega}_{60\text{ mT}}/dI_{\text{dc}} = 0.23 \pm 0.01\ \text{V}/A^2/\text{mA}$ at 60 mT, or in terms of modulation efficiency, $\eta^{2\omega}_{10mT} = 12.0 \pm 0.7\%/\text{mA}$ to $\eta^{2\omega}_{60mT} = 6.6 \pm 0.3\%/\text{mA}$. This result reveals a higher spin-current-controlled modulation for $|B| < 50$ mT, which disagrees with what we expect from Eq. (6).

B. Field dependence of the modulation efficiency

A magnetic-field-dependent measurement is performed for the 700-nm-wide Py modulator. Figure 4(a) shows the field scan of the $1f$ nonlocal resistance for different

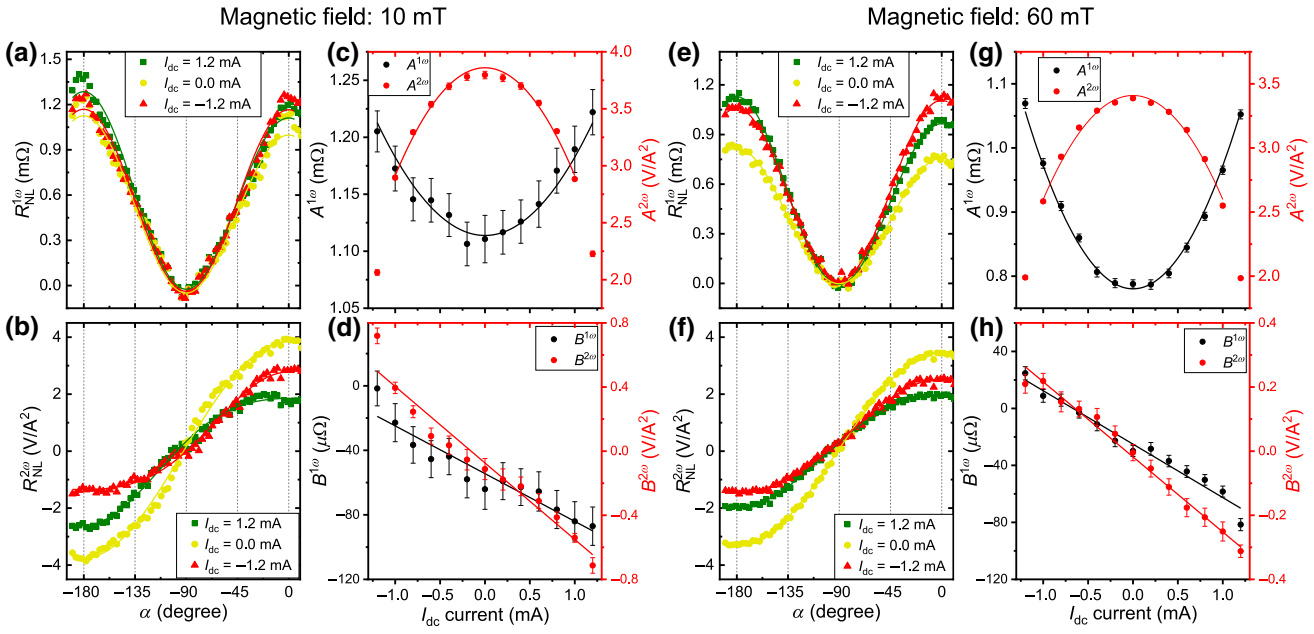

FIG. 3. (a),(b), [(e),(f)] Angular dependence of $1f$ and $2f$ of nonlocal resistances for a magnetic field of 10 mT [60 mT] for different modulator currents. (c),(d), [(g),(h)] Values of $A^{1\omega}$, $B^{1\omega}$, $A^{2\omega}$, and $B^{1\omega}$ at 10 mT [60 mT] as a function of the charge current in the modulator, from the best fit of Eq. (5) and (6). In our configuration, the positive modulator current produces a depletion of the magnon conductivity.

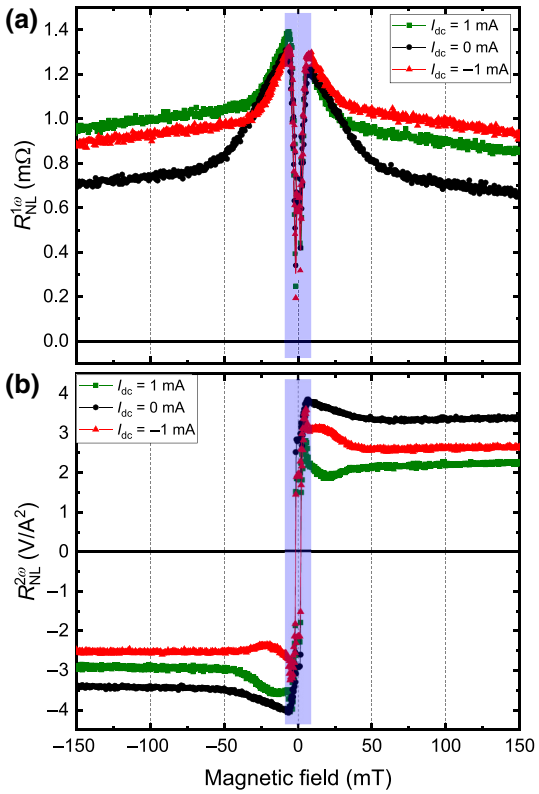

FIG. 4. (a) Magnetic field dependence of the $1f$ nonlocal resistance for different applied charge currents in the Py modulator. The asymmetry between positive and negative current corresponds to the spin-current-controlled modulation. (b) In the $2f$ response, the modulation generates a vertical shift between the positive and the negative currents.

applied currents in the modulator at $\alpha = 0°$. At $I_{dc} = 0$, the increase of nonlocal resistance below 50 mT occurs as a result of the MGE explained in Sec. III. However, when a charge current is applied at the modulator, two additional effects happen: (i) the nonlocal resistance increases proportional to the square of the I_{dc}, as shown in Figs. 3(c) and 3(g); (ii) the spin-current injection due to SHE and ASHE create an asymmetry between positive and negative magnetic fields, which is reversed by switching the charge current, as shown by the green and red curves in Fig. 4(a).

The modulation due to the MGE for either curves of $I_{dc} = \pm 1$ mA, decreases in comparison to the $I_{dc} = 0$ measurement, as well as, the magnitude of magnetic field necessary to align M_{Py} along B. This can be a signature of temperature dependency of the MGE caused by the Joule heating in the magnetic gate, decreasing the effectiveness of the MGE modulation. In order to investigate the heating effects in the $1f$ nonlocal resistance further, we subtract the nonlocal resistances with charge current of $I_{dc} = \pm 1$ mA, from the values obtained without an applied charge current, i.e., $[R_{NL}^{1\omega}(1\text{ mA}) - R_{NL}^{1\omega}(0\text{ mA})]$ and $[R_{NL}^{1\omega}(-1\text{ mA}) - R_{NL}^{1\omega}(0\text{ mA})]$, these curves are shown in Fig. 5(a). Despite the asymmetry between positive and negative current, Fig. 5(a) shows the enhancement of $R_{NL}^{1\omega}$ proportional to $I_{dc}{}^2$ at fields higher than 50 mT, also observed in the angular dependence measurements.

We can obtain the magnitude of the modulation from the field-dependency measurements by subtracting the nonlocal resistances measured with negative current compared to measured with positive current, i.e., $[R_{NL}^{1\omega}(-1\text{ mA}) - R_{NL}^{1\omega}(1\text{ mA})]$. However, in order to obtain the modulation efficiency, it is necessary to normalize this by the curve $R_{NL}^{1\omega}(0\text{ mA})$. Figure 5(b) shows the field dependency of the modulation efficiency. We observe a saturation of modulation efficiency around 50 mT, caused by the maximum contribution of the ASHE spin injection. Figure 5(b) is in agreement with the angular dependency analysis in Figs. 3(d) and 3(h).

The $2f$ nonlocal resistance as a function of the magnetic field for different applied charge currents is shown in Fig. 4 (b). The Joule heating decreases the nonlocal resistance, while the modulation due to the SHE and ASHE creates a split between positive current (green) and negative current (red) curves. The difference between positive and negative curves increase for $|B| < 50$ mT, indicating an increasing of the magnitude of the spin-current modulation. Figure 5(c) shows the modulation efficiency obtained similarly as the $1f$ in Fig. 5(b), i.e., taking the difference $[R_{NL}^{2\omega}(-1\text{ mA}) - R_{NL}^{2\omega}(1\text{ mA})]$ and normalized by $R_{NL}^{2\omega}(0\text{ mA})$. An enhancement of the spin-current modulation efficiency is obtained for $B < 50$ mT, confirming the different slopes for $B^{2\omega}$, shown in Figs. 3(d) and 3(h).

In order to explain the results, we look at the combination of three distinct effects, SHE, ASHE, and MGE. Differently for platinum, permalloy possesses the SHE and ASHE, thus $\mu_s^{Py} \equiv \mu_s^{SHE} + \mu_s^{ASHE}$. While μ_s^{SHE} in Py remains constant with respect to the magnetic field, i.e., Py magnetization, the contribution due to the ASHE depends on the relative angle between M_{Py} and charge-current direction. The results of the modulation efficiency for first-harmonic resistances confirms this statement, where we obtain an enhancement from 2.5 to 4.7% mA for low to high magnitude fields. Section III of the Supplemental Material shows a qualitative agreement between the field-dependency modulation of $1f$ and the $R_{NL}^{1\omega}$ shown in Fig. 6(a) [39].

On the other hand, the second-harmonic nonlocal resistances show an opposite behavior. The modulation efficiency by the charge current is 6.6% mA for $B = 60$ mT and 12% mA at 10 mT. That result disagrees with what is assumed in Eq. (6) and Ref. [17]. It is worthwhile emphasizing that, while for the first harmonic, the magnons diffuse from the injector to the detector, for the second harmonic, the detected voltage emerges from the thermally generated magnons, not only close to injector, but also nonlocally within the bulk region close to the detector

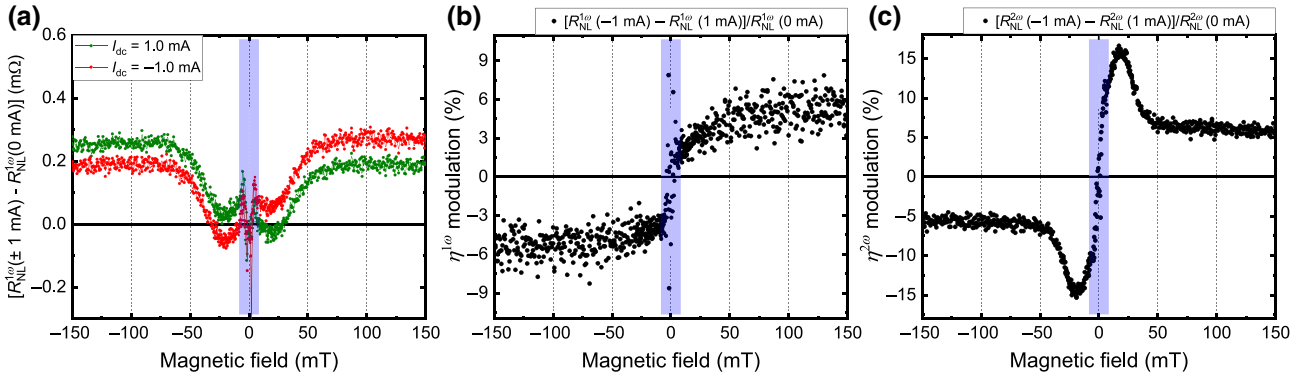

FIG. 5. (a) The difference of $\left[R_{\mathrm{NL}}^{1\omega}\ (1\ \mathrm{mA}) - R_{\mathrm{NL}}^{1\omega}\ (0\ \mathrm{mA})\right]$ and $\left[R_{\mathrm{NL}}^{1\omega}\ (-1\ \mathrm{mA}) - R_{\mathrm{NL}}^{1\omega}\ (0\ \mathrm{mA})\right]$ is plotted as a function of the magnetic field applied for $\alpha = 0^{\circ}$. (b) The magnetic field dependence of the magnon transport modulation efficiency for the $1f$ signal shows the enhancement of the modulation due to the ASHE contribution. (c) The $2f$ response shows an opposite behavior of the modulation efficiency.

[9,49,50]. Therefore, the magnon modulation due to SHE and ASHE may affect the first and second harmonic differently. While for the $1f$ all magnons that reach the detector cross the YIG-Py gate. In the $2f$ signals, just part of the thermally generated magnons are affected by the SHE and ASHE of the Py gate. Therefore, the results obtained in Fig. 5(c) may represent a competition between the SHE and ASHE modulation and MGE. Moreover, differently for the Pt modulator, the Joule heating in the permalloy can produce thermal magnons in the modulator, which may affect the magnon transport in the second-harmonic measurements, future experiments and finite-element modeling should explore the combination of those thermal effects.

Overall, the magnitude of the modulation efficiency obtained by using Py are comparable to the Pt modulator, confirming the potential and versatility of the magnetic gate in the magnon transport modulation. The results using Pt as modulator in the magnon transistor are shown in Sec. IV of the Supplemental Material [39].

V. CONCLUSIONS

In summary, we present a detailed investigation of the modulation of the magnon conductivity in YIG using a magnetic gate electrode Py. The modulation is estimated by means of nonlocal spin-transport measurements for different applied charge currents in the Py strip. By applying a charge current in the Py modulator, the nonlocal resistances show a combination of effects, namely the MGE and modulation by the SHE and the ASHE. The first-harmonic angular and field-dependent measurements show an enhancement of the modulation efficiency for fields higher than 50 mT, from $\eta_{10\,\mathrm{mT}}^{1\omega} = 2.5\%/\mathrm{mA}$ at 10 mT to $\eta_{60\,\mathrm{mT}}^{1\omega} = 4.7\%/\mathrm{mA}$ for 60 mT. The $1f$ results are in agreement with the expected ASHE contribution to the spin accumulation produced at the YIG-Py interface. However, the results of the thermally generated magnons disagree with that and show an opposite behavior. The maximum modulation efficiency occurs for $B < 50$ mT, where we find $\eta_{10\,\mathrm{mT}}^{2\omega} = 12\%/\mathrm{mA}$, while the minimum occurs at fields higher than 50 mT, $\eta_{60\,\mathrm{mT}}^{2\omega} = 6.6\ \%/\mathrm{mA}$. These results demonstrate that the ASHE in the permalloy layer plays a key role in the total spin accumulation, enabling it to be used as a magnetic modulator of the magnon spin conductivity in YIG. Moreover, due to the shape anisotropy, the magnon transport modulation efficiency can be controlled, turning on and off the ASHE component as a function of the magnetic field strength. We conclude that hybrid magnon structures, such as YIG-Py, represents a rich system to boost the paths towards the development of the magnon-based logic devices, not only from the perspective of combining the diverse branches of magnonic excitation, but also as we show, due to the multiple approaches to create and manipulate the transmission of magnons.

ACKNOWLEDGMENTS

We acknowledge the technical support from J.G. Holstein, T.J. Schouten, H. de Vries, F. A. van Zwol, and A. Joshua. We acknowledge the financial support of the Zernike Institute for Advanced Materials and the Future and Emerging Technologies (FET) programme within the Seventh Framework Programme for Research of the European Commission, under FET-Open Grant No. 618083 (CNTQC). This project is also financed by the NWO Spinoza prize awarded to Professor B.J. van Wees by the NWO.

APPENDIX: QUANTIFYING ASHE AND THE SHE COMPONENT IN THE 700-nm-WIDE Py STRIP

As a consequence of the shape anisotropy present on the Py strip, the contribution of the M_{Py}-dependent change to the spin conversion, i.e., ASHE, can be controlled by the

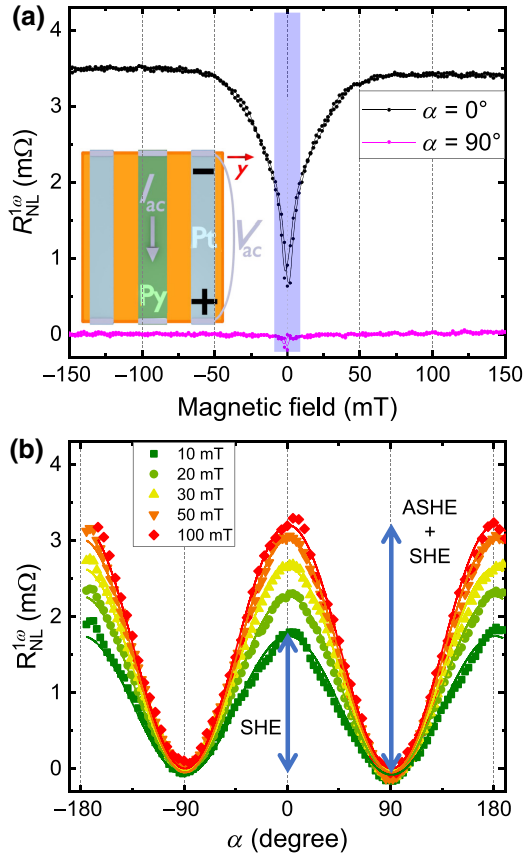

FIG. 6. (a) Magnetic field dependency of the nonlocal resistance using the middle Py strip as the injector. The inset shows the electrical connections used in these measurements. (b) Angular dependence of the $1f$ nonlocal resistances, showing the increase of the signal due to the contribution of the ASHE up to 50 mT.

external magnetic field. Qualitatively, the total spin accumulation created in the permalloy strip can be obtained by the first-harmonic response of the nonlocal resistance between the Pt and Py strips. Figures 6(a) and 6(b) show the field and angular dependency of the $1f$ response measured in the Pt detector strip using the middle 700-nm-wide Py strip as the injector. The inset in Fig. 6(a) shows the setup and connections used in this measurement. For $|B| <$ 10 mT, the spin injection is mainly due to the SHE component of Py [51]. However, $R_{NL}^{1\omega}$ increases for $|B| > 10$ mT and saturates around $B \approx 50$ mT, where the ASHE contribution is maximized due to the alignment of M_{Py} along the $\hat{y}$ axis, i.e., perpendicular to the charge current. The ratio between $1f$ nonlocal resistances at 60 and 10 mT correspond qualitatively to the spin accumulation at the YIG-Py interface caused by ASHE+SHE and SHE, respectively [23]. The obtained value is $R_{NL}^{1\omega}$ (60 mT)/$R_{NL}^{1\omega}$ (10 mT) $\approx$ 1.7. Therefore, an enhancement of the magnon transport modulation efficiency in the magnon transistor close to that value is expected for the first- and second-harmonic measurements. The shape anisotropy enables us to tune the magnon transport by turning the ASHE component on and off as a function of the magnetic field strength.

[1] S. A. Wolf, D. D. Awschalom, R. A. Buhrman, J. M. Daughton, S. von Molnár, M. L. Roukes, A. Y. Chtchelkanova, and D. M. Treger, Spintronics: A spin-based electronics vision for the future, Science **294**, 1488 (2001).

[2] Igor Žutić, Jaroslav Fabian, and S. Das Sarma, Spintronics: Fundamentals and applications, Rev. Mod. Phys. **76**, 323 (2004).

[3] Jairo Sinova, Sergio O. Valenzuela, J. Wunderlich, C. H. Back, and T. Jungwirth, Spin hall effects, Rev. Mod. Phys. **87**, 1213 (2015).

[4] A. A. Serga, A. V. Chumak, and B. Hillebrands, YIG magnonics, J. Phys. D **43**, 264002 (2010).

[5] V. V. Kruglyak, S. O. Demokritov, and D. Grundler, Magnonics, J. Phys. D **43**, 264001 (2010).

[6] B. Lenk, H. Ulrichs, F. Garbs, and M. Mnzenberg, The building blocks of magnonics, Phys. Rep. **507**, 107 (2011).

[7] A. V. Chumak, V. I. Vasyuchka, A. A. Serga, and B. Hillebrands, Magnon spintronics, Nat. Phys. **11**, 453 (2015).

[8] Arne Brataas, Bart van Wees, Olivier Klein, Grgoire de Loubens, and Michel Viret, Spin insulatronics, Phys. Rep. **885**, 1 (2020).

[9] L. J. Cornelissen, J. Liu, R. A. Duine, J. Ben Youssef, and B. J. van Wees, Long-distance transport of magnon spin information in a magnetic insulator at room temperature, Nat. Phys. **11**, 1022 (2015).

[10] Sebastian T. B. Goennenwein, Richard Schlitz, Matthias Pernpeintner, Kathrin Ganzhorn, Matthias Althammer, Rudolf Gross, and Hans Huebl, Non-local magnetoresistance in YIG/Pt nanostructures, Appl. Phys. Lett. **107**, 172405 (2015).

[11] Y. Kajiwara, K. Harii, S. Takahashi, J. Ohe, K. Uchida, M. Mizuguchi, H. Umezawa, H. Kawai, K. Ando, K. Takanashi, S. Maekawa, and E. Saitoh, Transmission of electrical signals by spin-wave interconversion in a magnetic insulator, Nature **464**, 262 (2010).

[12] Brandon L. Giles, Zihao Yang, John S. Jamison, and Roberto C. Myers, Long-range pure magnon spin diffusion observed in a nonlocal spin-Seebeck geometry, Phys. Rev. B **92**, 224415 (2015).

[13] L. J. Cornelissen, K. Oyanagi, T. Kikkawa, Z. Qiu, T. Kuschel, G. E. W. Bauer, B. J. van Wees, and E. Saitoh, Nonlocal magnon-polaron transport in yttrium iron garnet, Phys. Rev. B **96**, 104441 (2017).

[14] Devin Wesenberg, Tao Liu, Davor Balzar, Mingzhong Wu, and Barry L. Zink, Long-distance spin transport in a disordered magnetic insulator, Nat. Phys. **13**, 987 (2017).

[15] J. E. Hirsch, Spin Hall Effect, Phys. Rev. Lett. **83**, 1834 (1999).

[16] M. I. Dyakonov and V. I. Perel, Current-induced spin orientation of electrons in semiconductors, Phys. Lett. A **35**, 459 (1971).

[17] L. J. Cornelissen, J. Liu, B. J. van Wees, and R. A. Duine, Spin-Current-Controlled Modulation of the Magnon

Spin Conductance in a Three-Terminal Magnon Transistor, Phys. Rev. Lett. **120**, 097702 (2018).

[18] K. S. Das, F. Feringa, M. Middelkamp, B. J. van Wees, and I. J. Vera-Marun, Modulation of magnon spin transport in a magnetic gate transistor, Phys. Rev. B **101**, 054436 (2020).

[19] V. P. Amin, Junwen Li, M. D. Stiles, and P. M. Haney, Intrinsic spin currents in ferromagnets, Phys. Rev. B **99**, 220405(R) (2019).

[20] Angie Davidson, Vivek P. Amin, Wafa S. Aljuaid, Paul M. Haney, and Xin Fan, Perspectives of electrically generated spin currents in ferromagnetic materials, Phys. Lett. A **384**, 126228 (2020).

[21] Yasutomo Omori, Edurne Sagasta, Yasuhiro Niimi, Martin Gradhand, Luis E. Hueso, Fèlix Casanova, and Yoshi Chika Otani, Relation between spin Hall effect and anomalous Hall effect in 3*d* ferromagnetic metals, Phys. Rev. B **99**, 014403 (2019).

[22] K. S. Das, W. Y. Schoemaker, B. J. van Wees, and I. J. Vera-Marun, Spin injection and detection via the anomalous spin Hall effect of a ferromagnetic metal, Phys. Rev. B **96**, 220408(R) (2017).

[23] Kumar Sourav Das, Jing Liu, Bart J. van Wees, and Ivan J. Vera-Marun, Efficient injection and detection of out-of-plane spins via the anomalous spin hall effect in permalloy nanowires, Nano Lett. **18**, 5633 (2018).

[24] Joel Cramer, Andrew Ross, Samridh Jaiswal, Lorenzo Baldrati, Romain Lebrun, and Mathias Kläui, Orientation-dependent direct and inverse spin Hall effects in $Co_60Fe_20B_20$, Phys. Rev. B **99**, 104414 (2019).

[25] B. F. Miao, S. Y. Huang, D. Qu, and C. L. Chien, Inverse Spin Hall Effect in a Ferromagnetic Metal, Phys. Rev. Lett. **111**, 066602 (2013).

[26] A. Azevedo, O. Alves Santos, G. A. Fonseca Guerra, R. O. Cunha, R. Rodríguez-Suárez, and S. M. Rezende, Competing spin pumping effects in magnetic hybrid structures, Appl. Phys. Lett. **104**, 052402 (2014).

[27] Chunhui Du, Hailong Wang, Fengyuan Yang, and P. C. Hammel, Systematic variation of spin-orbit coupling with *d*-orbital filling: Large inverse spin Hall effect in 3*d* transition metals, Phys. Rev. B **90**, 140407(R) (2014).

[28] J. Ben Youssef, V. Castel, N. Vukadinovic, and M. Labrune, Spin-wave resonances in exchange-coupled Permalloy/garnet bilayers, J. Appl. Phys. **108**, 063909 (2010).

[29] A. Papp, W. Porod, and G. Csaba, Hybrid yttrium iron garnet-ferromagnet structures for spin-wave devices, J. Appl. Phys. **117**, 17E101 (2015).

[30] Jilei Chen, Chuanpu Liu, Tao Liu, Yang Xiao, Ke Xia, Gerrit E. W. Bauer, Mingzhong Wu, and Haiming Yu, Strong Interlayer Magnon-Magnon Coupling in Magnetic Metal-Insulator Hybrid Nanostructures, Phys. Rev. Lett. **120**, 217202 (2018).

[31] K. An, V. S. Bhat, M. Mruczkiewicz, C. Dubs, and D. Grundler, Optimization of Spin-Wave Propagation with Enhanced Group Velocities by Exchange-Coupled Ferrimagnet-Ferromagnet Bilayers, Phys. Rev. Appl. **11**, 034065 (2019).

[32] Zhizhi Zhang, Michael Vogel, José Holanda, Junjia Ding, M. B. Jungfleisch, Yi Li, John E. Pearson, Ralu Divan, Wei Zhang, Axel Hoffmann, Yan Nie, and Valentine Novosad, Controlled interconversion of quantized spin wave modes via local magnetic fields, Phys. Rev. B **100**, 014429 (2019).

[33] Yi Li, Wei Cao, Vivek P. Amin, Zhizhi Zhang, Jonathan Gibbons, Joseph Sklenar, John Pearson, Paul M. Haney, Mark D. Stiles, William E. Bailey, Valentine Novosad, Axel Hoffmann, and Wei Zhang, Coherent Spin Pumping in a Strongly Coupled Magnon-Magnon Hybrid System, Phys. Rev. Lett. **124**, 117202 (2020).

[34] Gershon Kurizki, Patrice Bertet, Yuimaru Kubo, Klaus Mølmer, David Petrosyan, Peter Rabl, and Jörg Schmiedmayer, Quantum technologies with hybrid systems, Proc. Natl. Acad. Sci. USA **112**, 3866 (2015).

[35] H. Wang, J. Chen, T. Yu, C. Liu, C. Guo, S. Liu, K. Shen, H. Jia, T. Liu, J. Zhang, and M. A. Cabero, Nonreciprocal coherent coupling of nanomagnets by exchange spin waves, Nano Res. 1 (2020).

[36] Yabin Fan, P. Quarterman, Joseph Finley, Jiahao Han, Pengxiang Zhang, J. T. Hou, Mark D. Stiles, A. J. Grutter, and Luqiao Liu, Manipulation of Coupling and Magnon Transport in Magnetic Metal-Insulator Hybrid Structures, Phys. Rev. Appl. **13**, 061002(R) (2020).

[37] Yuzan Xiong, Yi Li, Mouhamad Hammami, Rao Bidthanapally, Joseph Sklenar, Xufeng Zhang, Hongwei Qu, Gopalan Srinivasan, John Pearson, Axel Hoffmann, Valentine Novosad, and Wei Zhang, Probing magnon–magnon coupling in exchange coupled $Y_3Fe_5O_{12}$/Permalloy bilayers with magneto-optical effects, Sci. Rep. **10**, 12548 (2020).

[38] Y. Li, W. Zhang, V. Tyberkevych, W. K. Kwok, A. Hoffmann, and V. Novosad, Hybrid magnonics: Physics, circuits, and applications for coherent information processing, J. Appl. Phys. **128**, 130902 (2020).

[39] See Supplemental Material at http://link.aps.org/supplemental/10.1103/PhysRevApplied.15.014038 for sample fabrication details, permalloy width dependence of magnetic gating effect, comparative analysis between $R_{NL}^{1\omega}(H)$ and $\eta^{1\omega}(H)$ and the results of magnon transistor using platinum as modulator.

[40] A. Azevedo, L. H. Vilela Leão, R. L. Rodriguez-Suarez, A. B. Oliveira, and S. M. Rezende, dc effect in ferromagnetic resonance: Evidence of the spin-pumping effect?, J. Appl. Phys. **97**, 10C715 (2005).

[41] E. Saitoh, M. Ueda, H. Miyajima, and G. Tatara, Conversion of spin current into charge current at room temperature: Inverse spin-Hall effect, Appl. Phys. Lett. **88**, 182509 (2006).

[42] K. Uchida, J. Xiao, H. Adachi, J. Ohe, S. Takahashi, J. Ieda, T. Ota, Y. Kajiwara, H. Umezawa, H. Kawai, G. E. W. Bauer, S. Maekawa, and E. Saitoh, Spin Seebeck insulator, Nat. Mater **9**, 894 (2010).

[43] S. M. Rezende, R. L. Rodriguez-Suarez, R. O. Cunha, A. R. Rodrigues, F. L. A. Machado, G. A. Fonseca Guerra, J. C. Lopez Ortiz, and A. Azevedo, Magnon spin-current theory for the longitudinal spin-Seebeck effect, Phys. Rev. B **89**, 014416 (2014).

[44] Kevin S. Olsson, Kyongmo An, Gregory A. Fiete, Jianshi Zhou, Li Shi, and Xiaoqin Li, Pure Spin Current and Magnon Chemical Potential in a Nonequilibrium Magnetic Insulator, Phys. Rev. X **10**, 021029 (2020).

[45] L. J. Cornelissen and B. J. van Wees, Magnetic field dependence of the magnon spin diffusion length in the magnetic insulator yttrium iron garnet, Phys. Rev. B **93**, 020403(R) (2016).

[46] Joel Cramer, Lorenzo Baldrati, Andrew Ross, Mehran Vafaee, Romain Lebrun, and Mathias Kläui, Impact of electromagnetic fields and heat on spin transport signals in $Y_3Fe_5O_12$, Phys. Rev. B **100**, 094439 (2019).

[47] L. J. Cornelissen, J. Shan, and B. J. van Wees, Temperature dependence of the magnon spin diffusion length and magnon spin conductivity in the magnetic insulator yttrium iron garnet, Phys. Rev. B **94**, 180402(R) (2016).

[48] T. Wimmer, B. Coester, S. Geprgs, R. Gross, S. T. B. Goennenwein, H. Huebl, and M. Althammer, Anomalous spin Hall angle of a metallic ferromagnet determined by a multiterminal spin injection/detection device, Appl. Phys. Lett. **115**, 092404 (2019).

[49] Juan Shan, L. J. Cornelissen, Nynke Vlietstra, J. Ben Youssef, Timo Kuschel, R. A. Duine, and Bart J. van Wees, Influence of yttrium iron garnet thickness and heater opacity on the nonlocal transport of electrically and thermally excited magnons, Phys. Rev. B **94**, 174437 (2016).

[50] Y. Z. Cai, W. T. Li, Y. Wu, K. K. Meng, J. Miao, X. G. Xu, and Y. Jiang, Comparative measurements of local and nonlocal spin Seebeck effect in YIG/Pt nano-thick films, J. Magn. Magn. Mater. **476**, 166 (2019).

[51] Dai Tian, Yufan Li, D. Qu, S. Y. Huang, Xiaofeng Jin, and C. L. Chien, Manipulation of pure spin current in ferromagnetic metals independent of magnetization, Phys. Rev. B **94**, 020403(R) (2016).